Materials Today Communications 53 (2026) 115346

Contents lists available at ScienceDirect

Materials Today Communications

journal homepage: www.elsevier.com/locate/mtcomm

Global sensitivity analysis of Rayleigh wave propagation in functionally graded skin tissue: A fractional three-phase lag thermo-viscoelastic model

Maaz Ali Khan [a,*], Khadijah M. Abualnaja [c], Adnan Jahangir [b], Emad E. Mahmoud [c], Usman Riaz [a], Murat Yaylacı [d]

[a] Department of Physical and Numerical Sciences, Qurtaba University of Science and Information Technology, Peshawar, Pakistan
[b] Department of Mathematics, COMSATS University Islamabad, Wah Campus, Pakistan
[c] Department of Mathematics and Statistics, Collage of Science, Taif University, P.O. Box 11099, Taif 21944, Saudi Arabia
[d] Department of Civil Engineering, Recep Tayyip Erdogan University, Rize 53100, Türkiye

ARTICLE INFO

Keywords:
Rayleigh waves
Skin tissue
Sensitivity analysis
Bioheat transfer
Functionally graded
Fractional thermoelasticity

ABSTRACT

The paper develops a complete fractional three-phase lag thermo-viscoelastic model in order to investigate Rayleigh wave propagation in the functionally graded human skin tissue. The proposed framework combines nonlocal elasticity, fractional memory effects, and depth-dependent material gradation-a key lacuna in the integration of multi-physics into biological wave modeling. Furthermore, it conducts the GSA using the variance-based Sobol method to quantify the influence of primary parameters, namely elastic nonlocality (ϵ_1), thermal nonlocality (ϵ_2), fractional order (α), gradation parameter (α^*), phase lags (τ_q, τ_T, τ_v), and hydrostatic stress (P) on phase velocity, attenuation, penetration depth, and specific heat loss. All phase velocities are normalized by a reference speed $c_0 = 10 \quad m/s$ (typical for skin) to present dimensionless results; the corresponding physical values lie in the range $100 - 1000 m/s$, consistent with elastography measurements. Results have demonstrated that wave characteristics are mainly controlled by thermal nonlocality (ϵ_2) with respect to heat loss, the fractional order (α) for penetration depth, while elastic nonlocality (ϵ_1) for phase velocity, and attenuation is the result of very complex synergistic interactions of all parameters. Herein, GSA provides a sound hierarchy for model simplification and parameter prioritization, providing needed insight into optimizing diagnostic elastography and thermal therapies in clinical applications.

1. Introduction

Elastodynamics, being a separate branch of continuum mechanics, studies the complex behavior of elastic materials under dynamic loading, specifically for wave propagation and temporally dependent response of materials. The discipline is fundamental to the elucidation of propagation and interaction of mechanical waves including body and surface waves in the solid medium. The underpinnings of the theory stem from the principles of stress, strain and energy conservation. Elasticodynamic theory has been developed over 150 years or more; the theoretical formulations in the long wavelength regime have been fundamentally proved by experimental investigation. Today, dynamic elasticity theory is indispensable in many branches of engineering and science in the context of mechanical vibrations, impact loading, geophysics, seismology and biophysics [1].

The propagation of surface waves (e.g., Rayleigh, Love, and Stoneley waves) is a major subject in the field of elastodynamics, especially with applications on biological tissues (e.g., human skin) [2]. These waves exhibit unique propagation properties along interfaces in materials or within the surface layers. Rayleigh waves, for example, involve elliptical particle motion at the surface and have a high sensitivity for surface properties, thus becoming a valuable tool for non-invasive diagnostic methods (e.g. ultrasound elastography). Love waves are horizontally polarized shear waves in layered structures while Stoneley waves are at the edge of two solids and depend on the properties of the two mediums.

Successive refinements to the coupled thermoelasticity theory have occurred in the course of its development. While classical elasticity is quite adequate for isothermal conditions, it excludes thermal effects-a serious deficiency when dealing with biological tissues. Biot [3] developed the theory of coupled thermoelasticity based on the heat conduction law by Fourier and the equations of motion. This model, however, still possessed the infinite speed of thermal waves. To overcome this

* Corresponding author.
E-mail address: maazali977@gmail.com (M.A. Khan).

https://doi.org/10.1016/j.mtcomm.2026.115346
Received 18 February 2026; Received in revised form 4 April 2026; Accepted 7 May 2026
Available online 9 May 2026

defect, Cattaneo [4] and Vernotte [5] developed the hyperbolic heat conduction model, which assured finite speeds of propagation.

Further generalizations included the Lord–Shulman (LS) model with one relaxation time [6], and the Green–Lindsay (GL) model with two relaxation times [7]. Tzou [8,9] further developed the Dual-phase-lag (DPL) and in turn three-phase-lag (TPL) models that incorporate the interactions due to microstructural effects. Simultaneously, Green and Naghdi GN proposed three thermoelastic models GN-I, GN-II, GN-III based on entropy balance and thermal displacement. The last-mentioned model, GN-III, was associated with dissipative processes [10–12]. Roy Choudhuri [13] extended such ideas to a complete three-phase-lag theory incorporating lags due to heat flux, temperature gradient, and thermal displacement.

In recent decades, fractional calculus has been incorporated into thermoelasticity, allowing the modeling of memory effects and anomalous behavior [14,15]. Ezzat et al. [16] developed fractional-order TPL models, while various authors have utilized fractional derivatives in wave propagation in non-local and viscoelastic media [17,18]. Biomechanical applications have involved thermoelastic models to study laser-tissue interactions [19,20], wave propagation in non-local media with voids [21,22], and surface wave techniques for tissue characterization [22–29]. For example, Grinspan et al. [23] investigated skeletal muscles using surface wave elastography, while Han et al. [27] used optical coherence elastography with Rayleigh wave models to quantify tissue viscoelasticity.

In related recent developments, Gupta et al. [30] investigated deformation in a rotating functionally graded double porous thermoelastic medium under Green–Naghdi III theory, demonstrating the combined influence of gravity, magnetic field, and thermal shock on various physical fields. In another study, Gupta et al. [31] analyzed photothermal excitation in a nonlocal semiconducting double porous medium using fractional triple-phase-lag theory, revealing the significant roles of nonlocality, initial stress, and thermoelectric coupling. Further developments by Gupta et al. [32] and Das et al. [33] incorporated fractional MGT models, memory-dependent heat transport, and nonlocal elasticity to study Rayleigh waves and coupled hydro-thermo-electromechanical responses, emphasizing the effects of porosity, delay parameters, and size-dependence. Additionally, Sur et al. [34] employed an advanced finite element framework to examine photothermal behavior in cylindrical semiconductors with spatial nonlocality and memory-dependent heat transport, highlighting the sensitivity of physical fields to time-delay effects and the importance of nonlocal interactions in thermoelastic analysis.

Despite these contributions, several critical gaps persist that this study directly addresses:

1. **Limited multi-physics**: Current models rarely incorporate the physics of fractional heat conduction, non-local elasticity (Eringen's theory), viscoelasticity, and material gradation of biological tissues into one framework [35].
2. **Oversimplification of skin properties**: Skin is often modeled as a homogeneous, temperature insensitive material. Its layered architecture, viscoelastic behavior, and thermally responsive nature are neglected [27,28].
3. **Limited sensitivity analyses**: Few studies conduct thorough local and global sensitivity analyses [36] to identify the dominant parameters that control wave propagation in skin, which is very important for the validation of these models and clinical translation.

To fill these gaps, we present the first integrated framework that simultaneously combines fractional three-phase-lag heat conduction, Eringen's nonlocal elasticity, viscoelasticity, lateral functional gradation, and the Pennes bioheat equation for human skin. In addition, we perform a rigorous global sensitivity analysis using Sobol indices to rank parameter importance – an approach not previously applied to Rayleigh waves in skin. The novelty is underlined by comparison with recent relevant studies: Biswas & Mukhopadhyay [24] considered nonlocal thermoelasticity without fractional derivatives or gradation; Zhang et al. [20] analyzed wave propagation in graded viscoelastic media without thermal effects; Khan et al. [37] performed sensitivity analysis on surface waves; Khan et al. [29] examined nonlocal bioheat transfer without wave propagation. None combine all the features of our model. The objectives of this study are threefold: (i) to formulate an integrated platform based on the fractional three-phase lag heat conduction model, Eringen's nonlocal elasticity, and material gradation to adequately model the skin's layering, dissipative, and memory-dependent properties; (ii) to determine the governing dispersion relation and develop a parametric analysis with regards to fractional order, nonlocal effects, gradation, and hydrostatic stress; and (iii) to carry out a rigorous global sensitivity analysis by ranking the influence of all the aforementioned parameters and identifying the dominating mechanism. The research has filled the gap between the advanced thermoelastic theory and the practical biomedical applications by providing a refined interpretation tool for diagnostic elastography data and optimization of safety in thermal-based therapies.

2. Mathematical formulation

2.1. Constitutive relations with non-local elasticity

The skin tissue is modeled as a homogeneous, isotropic, thermo-viscoelastic half-space with non-local effects. According to Eringen's non-local elasticity theory [38], the constitutive relation for a thermo-viscoelastic material can be expressed as:

$$\left(1-\epsilon_1{}^2\nabla^2\right)\sigma_{ij} = -P\left(\delta_{ij}+\omega_{ij}\right)+\left\{2\overline{\mu}e_{ij}+\ \left(\overline{\lambda}e_{rr}-\overline{\gamma}T\right)\delta_{ij}\right\} \tag{1}$$

sssssse:

- σ_{ij} is the Cauchy stress tensor
- $e_{ij}=\frac{1}{2}(u_{i,j}+u_{j,i})$ is the strain tensor
- u_i are displacement components
- T is temperature variation from reference T_0
- δ_{ij} is Kronecker delta
- ϵ_1 is the **elastic non-local parameter** accounting for long-range interactions
- P is the hydrostatic stress
- $\omega_{ij}=\frac{1}{2}\left(u_{j,i}-u_{i,j}\right)$ is the rotational tensor and this term represents the local rigid-body rotation of the medium.

The viscoelastic effect that we have [29],

$$\begin{pmatrix}\overline{\lambda}\\ \overline{\mu}\\ \overline{\gamma}\\ \overline{k}\\ \overline{k^*}\end{pmatrix}=\begin{pmatrix}\lambda\\ \mu\\ \gamma\\ k\\ k^*\end{pmatrix}^R+i\omega\begin{pmatrix}\lambda\\ \mu\\ \gamma\\ k\\ k^*\end{pmatrix}^I, \tag{2}$$

2.2. Equation of motion

The equation of motion neglecting body forces is [14]:

$$\sigma_{ij,j}=\rho\ddot{u}_i \tag{3}$$

where ρ is tissue density, u_i is the displacement component and dots denote time differentiation.

2.3. Generalized bioheat equation

The energy conservation equation for biological tissue, incorporating perfusion and metabolic effects is [29]:

$$\rho_t c_t \frac{\partial T}{\partial t} + \overline{\gamma} T_0 \nabla . \frac{\partial \boldsymbol{u}}{\partial t} = -\nabla . \boldsymbol{q} + \omega_b \rho_b c_b (T_b - T) + Q \tag{4}$$

where:

- ρ_t, c_t are tissue density and specific heat
- $\overline{\gamma} = \gamma + i\omega\gamma^*$ is complex thermoelastic coupling constant
- **q** is heat flux vector
- ω_b, ρ_b, c_b are blood perfusion rate, density, and specific heat
- T_b is arterial blood temperature
- Q is metabolic heat generation

2.4. Three-phase-lag heat conduction with fractional derivatives

The heat flux vector is defined by [37],

$$\boldsymbol{q} = -(k\nabla \mathrm{T} + \mathrm{k}^* \nabla v)$$

where **q** denotes the heat flux, T is the temperature, v represents the thermal displacement, k is the thermal conductivity, and k^* is the rate of thermal conductivity. According to the Green–Naghdi type II thermoelastic theory, the thermal conductivity rate k^* is expressed as,

$$k^* = \frac{c_t(\lambda + 2\mu)}{4},$$

with $c_t$being the thermal wave speed, and λ and μ denoting Lamé's constants.

To incorporate both local and nonlocal thermal effects, the heat conduction equation can be written in the form [25]

$$(1 - \epsilon_2^2 \nabla^2)\boldsymbol{q} = -(\overline{k}\nabla T + \overline{k}^* \nabla v),$$

where ϵ_2 is the thermal nonlocal parameter.

Expanding this relation within the framework of the three-phase-lag heat conduction model yields [37],

$$\left(1 + \tau_q \frac{\partial}{\partial t}\right)(1 - \epsilon_2^2 \nabla^2)\boldsymbol{q} = -\left[\overline{k}\left(1 + \tau_T \frac{\partial}{\partial t}\right)\nabla T + \overline{k}^* \left(1 + \tau_v \frac{\partial}{\partial t}\right)\nabla v\right] \tag{5}$$

where:

- τ_q is heat flux phase lag
- τ_T is temperature gradient phase lag
- τ_v is thermal displacement gradient phase lag
- k, k^* are thermal conductivity coefficients

To incorporate **memory effects**, we employ Caputo fractional derivatives of order $\alpha (0 < \alpha \leq 1)$:

$${}^{c}D^{\alpha} f(t) = \frac{1}{\Gamma(1-\alpha)} \int_0^t \frac{f'(\tau)}{(t-\tau)^{\alpha}}\, d\tau. \tag{6}$$

The fractional-order TPL heat conduction equation with the Caputo derivative and the Bioheat equation becomes [29];

$$\tau_q^* \left(1 - \epsilon_2^2 \nabla^2\right)\left(\rho_t c_t \frac{\partial^2 \theta}{\partial t^2} + \overline{\gamma} T_0 \nabla \frac{\partial^2 u}{\partial t^2} + \omega_b \rho_b c_b \frac{\partial \theta}{\partial t}\right) = k^* \left[\left(\tau_k + \tau_k \tau_T^* + \tau_v^*\right)\nabla^2 \dot{\theta} + \nabla^2 \theta\right] \tag{7}$$

where:

- $\theta = T - T_0$ is temperature variation
- ϵ_2 is **thermal non-local parameter**
- $\tau_k = k/k^*$

Fractional operators are defined as:

$$\tau_q^* = 1 + \frac{\tau_q^{\alpha}}{\alpha!}\frac{\partial^{\alpha}}{\partial t^{\alpha}} + \frac{\tau_q^{2\alpha}}{(2\alpha)!}\frac{\partial^{2\alpha}}{\partial t^{2\alpha}}; \tau_T^* = \frac{\tau_T^{\alpha}}{\alpha!}\frac{\partial^{\alpha}}{\partial t^{\alpha}}; \tau_v^* = k + k^* \frac{\tau_v^{\alpha}}{\alpha!}\frac{\partial^{\alpha-1}}{\partial t^{\alpha-1}}.$$

3. Problem solution

3.1. Problem statement and assumptions

A Cartesian coordinate system (x,y,z) is introduced such that the skin surface is located at $z = 0$, while the underlying tissue occupies the semi-infinite region $z \geq 0$. Rayleigh waves are assumed to travel along the positive x-direction on the surface (Fig. 1).

In a functionally graded medium, the material properties are not uniform but vary smoothly with position. Such spatial variation is especially important when studying surface waves, since even mild inhomogeneity along the direction of propagation can noticeably affect stress distribution and wave characteristics. Unlike most studies that assume depth-dependent gradation, we consider lateral gradation along the propagation direction x. This choice is physiologically relevant for conditions such as wound healing, tumor growth, or stretch marks, where stiffness varies significantly over the skin surface. If this gradation is ignored, the resulting wave model may fail to capture the actual mechanical response of the medium [37].

$$(\overline{\lambda}, \quad \overline{\mu}, \quad \overline{\gamma}, \overline{k}, \quad \overline{k}^*) = g(x) \times (\overline{\lambda}_0, \quad \overline{\mu}_0, \quad \overline{\gamma}_0, \overline{k}_0, \quad \overline{k}_0^*) \tag{8}$$

The condition (8) modifies the Eqs. (1,3,7) as follows,

$$\left(1 - \epsilon_1{}^2 \nabla^2\right)\sigma_{ij} = -P(\delta_{ij} + \omega_{ij}) + \left[2\overline{\mu}_0 e_{ij} + \left(\overline{\lambda}_0 e_{rr} - \overline{\gamma}_0 T\right)\delta_{ij}\right] \times g(x) \tag{9}$$

$$\sigma_{ij,j} = \left(1 - \epsilon_1{}^2 \nabla^2\right) \times \left[\left[-P(\delta_{ij} + \omega_{ij})\right] + \left[2\overline{\mu}_0 e_{ij} + \left(\overline{\lambda}_0 e_{rr} - \overline{\gamma}_0 T\right)\delta_{ij}\right] \times g(x)\right] = \rho \ddot{u}_i \tag{10}$$

$$\tau_q^* \left(1 - \epsilon_2^2 \nabla^2\right)\left(\rho_t c_t \frac{\partial^2 \theta}{\partial t^2} + g(x)\overline{\gamma}_0 T_0 \nabla \frac{\partial^2 u}{\partial t^2} + \omega_b \rho_b c_b \frac{\partial \theta}{\partial t}\right) = g(x) k_0^* \left[\left(\tau_k + \tau_k \tau_T^* + \tau_v^*\right)\nabla^2 \dot{\theta} + \nabla^2 \theta\right] \tag{11}$$

To account for this effect in a simple and tractable way, the material parameters are assumed to vary along the x-direction through an exponential grading function. Accordingly, the functional gradation is represented by $g(x) = e^{\alpha^* x}$, where $\alpha^*$is the inhomogeneity parameter governing the rate of spatial variation. This choice preserves analytical simplicity while effectively incorporating the influence of material gradation on Rayleigh wave propagation. Tests with power-law gradation show qualitatively identical sensitivity rankings (difference < 5% in phase velocity).

Due to the plane strain assumption, all mechanical and thermal field variables are taken to be independent of the y-coordinate. Accordingly, the displacement vector is confined to the x–z plane and is expressed as

$$u = (u, 0, w)(x, z, t) \tag{12}$$

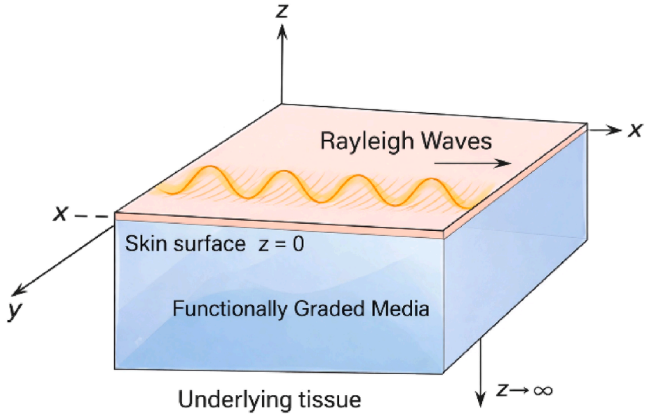

Fig. 1. Rayleigh wave propagation in human skin tissue.

Using Eq. (12) in Eq. (9-11), yields,

$$\left[\left(-P+(\bar{\lambda}_0+2\bar{\mu}_0)\times e^{\alpha^* x}\right)\frac{\partial^2 u}{\partial x^2}+\left((\bar{\lambda}_0+\bar{\mu}_0)\alpha^* e^{\alpha^* x}\right)\frac{\partial u}{\partial x}+\left(\frac{-P}{2}+(\bar{\lambda}_0+\bar{\mu}_0)e^{\alpha^* x}\right)\frac{\partial^2 w}{\partial x\partial z}+\alpha^*\bar{\lambda}_0 e^{\alpha^* x}\frac{\partial w}{\partial z}\right]\left[+\left(\frac{-P}{2}+2\bar{\mu}_0 e^{\alpha^* x}\right)\frac{\partial^2 u}{\partial z^2}-\alpha^* e^{\alpha^* x}\bar{\gamma}_0 T-\bar{\gamma}_0 e^{\alpha^* x}\frac{\partial\theta}{\partial x}\right]$$
$$=\rho\frac{\partial^2 u}{\partial t^2}-\rho\varepsilon_1^2\frac{\partial^4 u}{\partial x^2\partial t^2}-\rho\varepsilon_1^2\frac{\partial^4 u}{\partial z^2\partial t^2} \tag{13}$$

$$\left[\left(\frac{-P}{2}+2\bar{\mu}_0 e^{\alpha^* x}\right)\frac{\partial^2 w}{\partial x^2}+\left(\frac{-P}{2}+(\bar{\lambda}_0+2\bar{\mu}_0)e^{\alpha^* x}\right)\frac{\partial^2 u}{\partial x\partial z}+\alpha^* 2\bar{\mu}_0 e^{\alpha^* x}\frac{\partial w}{\partial x}+\alpha^* 2\bar{\mu}_0 e^{\alpha^* x}\frac{\partial u}{\partial z}\right]\left[+\left(-P+(\bar{\lambda}_0+2\bar{\mu}_0)e^{\alpha^* x}\right)\frac{\partial^2 w}{\partial z^2}-\bar{\gamma}_0 e^{\alpha^* x}\frac{\partial\theta}{\partial z}\right]$$
$$=\rho\frac{\partial^2 w}{\partial t^2}-\rho\varepsilon_1^2\frac{\partial^4 w}{\partial x^2\partial t^2}-\rho\varepsilon_1^2\frac{\partial^4 w}{\partial z^2\partial t^2} \tag{14}$$

$$\tau_q^*\left[\left(\rho_t c_t\frac{\partial^2\theta}{\partial t^2}+\bar{\gamma}_0 T_0\left(\frac{\partial^3 u}{\partial t^2\partial x}+\frac{\partial^3 w}{\partial t^2\partial z}\right)\times e^{\alpha^* x}\right)+\omega_b\rho_b c_b\frac{\partial\theta}{\partial t}\right]-$$
$$\tau_q^*\varepsilon_2^2\left[\left(\rho_t c_t\frac{\partial^4\theta}{\partial t^2\partial x^2}+\alpha^*\bar{\gamma}_0 T_0\left(\frac{\partial^5 u}{\partial t^2\partial x^3}+\frac{\partial^5 w}{\partial t^2\partial x^2\partial z}\right)e^{\alpha^* x}+\bar{\gamma}_0 T_0\left(\frac{\partial^5 u}{\partial t^2\partial x^3}+\frac{\partial^5 w}{\partial t^2\partial x^2\partial z}\right)e^{\alpha^* x}\right)+\omega_b\rho_b c_b\frac{\partial^3\theta}{\partial t\partial x^2}\right]$$
$$-\tau_q^*\varepsilon_2^2\left[\left(\rho_t c_t\frac{\partial^4\theta}{\partial t^2\partial z^2}+\bar{\gamma}_0 T_0\left(\frac{\partial^5 w}{\partial t^2\partial z^3}+\frac{\partial^5 u}{\partial t^2\partial z^2\partial x}\right)e^{\alpha^* x}\right)+\omega_b\rho_b c_b\frac{\partial^3\theta}{\partial t\partial z^2}\right]=$$
$$e^{\alpha^* x}\times k_0^*\left[\left(\tau_k+\tau_k\tau_T^*+\tau_v^*\right)\left(\frac{\partial^3\theta}{\partial x^2\partial t}+\frac{\partial^3\theta}{\partial z^2\partial t}\right)+\left(\frac{\partial^2\theta}{\partial x^2}+\frac{\partial^2\theta}{\partial z^2}\right)\right] \tag{15}$$

3.2. Solution of the problem

Assuming time-harmonic solutions of the form [33];

$$\Xi=\Xi^*\, e^{i\xi(x+mz-ct)} \tag{16}$$

where:

- $\Xi=(u,w,\theta)$

where ξ is the **complex** wavenumber ($\xi=\xi_R+i\xi_I$), c is the phase velocity, and m governs depth decay. **Attenuation definition:** The spatial attenuation along the propagation direction x is given by $\alpha_{\text{att}}=\xi_I$ (nepers/m). The dimensionless attenuation factor plotted in the figures is AF $=\xi_I/\xi_R$. The penetration depth is $\delta=1/|\xi_I|$.

3.3. Governing equations in terms of potentials

Substituting Eq. (16) into Eqs. (13–15) and eliminating stresses yields three coupled equations:

$$\left(a_1+a_2m^2\right)u^*+a_3mw^*-a_4\theta^*=0 \tag{17}$$

$$a_5mu^*+\left(a_6+a_7m^2\right)w^*-a_8m\theta^*=0 \tag{18}$$

$$\left(a_9+a_{10}m^2\right)u^*+\left(a_9m+a_{10}m^3\right)w^*+\left(a_{11}+a_{12}m^2\right)\theta^*=0 \tag{19}$$

For completeness, the coefficients a_1-a_{12} are in Appendix-I.

3.4. Characteristic equation

For non-trivial solutions, the determinant of the coefficient matrix must vanish, yielding:

$$Am^6+Bm^4+Cm^2+D=0 \tag{20}$$

For completeness, the coefficients A–D from the characteristic equation are provided in the Appendix-I.

3.5. General solution form

Eq. (20) yields six roots m_j ($j=1,2,3,4,5,6$), of which three with $\Re(m_j)\geq 0$ correspond to surface waves decaying with depth. The general solution is:

$$\Xi=\begin{pmatrix}1\\ d_j\\ l_j\end{pmatrix}A_j e^{-m_j z}e^{i\xi(x-ct)} \tag{21}$$

where A_j are constants determined from boundary conditions, and:

$$d_j=\frac{-a_{14}m^3-a_{13}m}{a_{16}m^2+a_{15}}; \tag{22}$$

$$l_j=\frac{a_{17}m^6+a_{18}m^4+a_{19}m^2+a_{20}}{a_{21}m^4+a_{22}m^2+a_{23}} \tag{23}$$

$$a_{13}=a_1a_8-a_4a_5; a_{14}=a_8a_2; a_{15}=-a_4a_6; a_{16}=(a_8a_3-a_4a_7); a_{17}=a_{14}a_{10};$$

$$a_{18}=-a_{16}a_{10}+a_{13}a_{10}+a_{14}a_9; a_{19}=-a_{15}a_{10}-a_9a_{16}+a_{13}a_9; a_{20}=-a_9a_{15};$$

$$a_{21}=a_{16}a_{12}; a_{22}=a_{15}a_{12}+a_{11}a_{16}; a_{23}=a_{15}a_{11}.$$

3.6. Boundary conditions

At the stress-free, thermally regulated surface $z=0$:

$$\sigma_{zz}=0; \sigma_{xz}=0. \tag{24}$$

$$\frac{\partial\Theta}{\partial z}+h\Theta=0\rightarrow z=0, \tag{25}$$

where:

- $h\rightarrow 0$ represents **insulated boundary**
- $h\rightarrow\infty$ represents **isothermal boundary**

3.7. Secular equation

Applying the boundary conditions yields a homogeneous system:

$$\sum_{j=1}^{3}k_{ij}A_j=0; \tag{26}$$

$$K_{1j}=\left(-P-(\bar{\lambda}_0+2\bar{\mu}_0+P)(i\xi)m_j d_j e^{\alpha^* x}+\bar{\lambda}_0 i\xi e^{\alpha^* x}-\bar{\gamma}_0 l_j e^{\alpha^* x}\right)=0, \tag{27}$$

$$K_{2j}=\left(\frac{-P}{2}+e^{\alpha^* x}-\bar{\mu}_0\right)\left(m_j+d_j\right)(i\xi)=0, \tag{28}$$

$$K_{3j}=\left(-i\xi m_j+h\right)l_j=0. \tag{29}$$

For non-trivial A_j, the determinant must vanish:

$$\det\left(K_{ij}\right)=0 \tag{30}$$

Eq. (30) is the **secular equation** whose solution gives the dispersion relation $c=c(\xi)$ and other wave characteristics.

4. Global sensitivity analysis (GSA)

Global sensitivity analysis is conducted to quantify the influence of uncertain input parameters on the thermo-viscoelastic wave response in skin tissue. In contrast to local sensitivity methods, which examine perturbations around a nominal point, GSA explores the full admissible parameter space and is therefore more appropriate for nonlinear and coupled multiphysics systems, where parameter interactions play a significant role [39].

In this study, a variance-based Sobol framework is employed to decompose the total variance of the model output into contributions arising from individual input parameters and their higher-order interactions. This approach enables a comprehensive assessment of both main and interaction effects.

4.1. Problem formulation

Let the model output be expressed as

$$Y = f(X_1, X_2, \ldots, X_n),$$

where $X_i, i = 1, 2, \ldots, n$, denote independent input parameters assumed to be uniformly distributed over the unit hypercube $[0,1]^n$. Under the assumption of square-integrability, $f(X) \in L^2([0,1]^n)$, the function can be decomposed using the Sobol–Hoeffding expansion as [28],

$$f(X) = f_0 + \sum_{i=1}^{n} f_i(X_i) + \sum_{i<j}^{n} f_{ji}\left(X_i, X_j\right) + \ldots + f_{1,2,\ldots n}\left(X_1, X_2, \ldots, X_n\right) \quad (31)$$

subject to orthogonality conditions ensuring uniqueness of the decomposition. The component functions are defined through conditional expectations as

$$f_0 = E(H) \quad (32)$$

$$f_j(X_j) = E(H|X_j) - f_0 \quad (33)$$

$$f_{ji}(X_j, X_i) = E(H|X_j, X_i) - f_0 - f_j - f_i \quad (34)$$

with higher-order terms defined analogously. Integrating the squared expansion over the input domain yields the variance decomposition

$$Var(Y) = \sum_{i=1}^{n} V_i + \sum_{i<j}^{n} V_{ij} + \ldots + V_{1,2,\ldots,n}. \quad (35)$$

where each term represents the contribution of individual parameters and their interactions to the total variance.

4.2. First-order sensitivity indices

The first-order sensitivity index (main effect index) for parameter X_i is defined as,

$$S_i = \frac{\mathrm{Var}_{X_{\sim i}}(\mathbb{E}(Y|X_{\sim i}))}{\mathrm{Var}(Y)} \quad (36)$$

This index measures the isolated contribution of X_i to the output variance, averaged over all other parameters. The indices satisfy,

$$\sum_{i=1}^{n} S_i \leq 1, \quad (37)$$

with equality holding for purely additive models without interactions.

4.3. Total-effects index

To account for all interaction effects involving a given parameter, the total-effect sensitivity index is defined as [28]

$$S_{T_i} = 1 - \frac{\mathrm{Var}_{X_{\sim i}}(\mathbb{E}(Y|X_{\sim i}))}{\mathrm{Var}(Y)}. \quad (38)$$

where $X_{\sim i}$ denotes the set of all input parameters except X_i. In general, $S_{T_i} \geq S_i$, and the difference between these indices reflects the contribution of interaction effects associated with X_i.

4.4. Computational procedure

The Sobol indices are estimated using a Monte Carlo sampling approach based on Latin Hypercube Sampling:

- Two independent sample matrices $A$and $B$of size $N \times L$are generated, where $N = 10^4$ and $L = 8$ denotes the number of input parameters.
- The corresponding model outputs are computed as

$$Y_A = f(A), Y_B = f(B).$$

- For each parameter i, a hybrid matrix C_i is constructed by replacing the i-th column of $A$with that of B, and the output is evaluated as

$$Y_{C_i} = f(C_i).$$

The sensitivity indices are then estimated using Jansen's estimators:

$$S_i = \frac{\mathbb{E}[Y_B(Y_{C_i} - Y_A)]}{\mathrm{Var}(Y)},$$

$$S_{T_i} = \frac{\mathbb{E}[(Y_A - Y_{C_i})^2]}{2\,\mathrm{Var}(Y)}.$$

These expressions provide robust and efficient estimates of both first-order and total-effect indices.

4.5. Simulation setup and outputs

Each input parameter is varied within ±10% of its nominal value. For the considered eight input parameters and four output quantities of interest phase velocity, attenuation coefficient, penetration depth, and specific heat loss a total of twenty-four sensitivity responses is obtained. To facilitate comparison, the mean absolute values of the sensitivity indices are computed and analyzed. The results, presented in Figs. 14–15, highlight the relative importance of each parameter and provide insight into the dominant factors governing the thermo-viscoelastic wave behavior in the present model (Table 1).

4.6. Convergence and sampling

Convergence was verified by increasing N from 2×10^3 to 2×10^4. At $N = 10^4$, all indices changed by $< 1\%$ upon doubling. Final $N = 10^4$. Total model evaluations per QoI: $N(L+2) = 10^4 \times (8+2) = 10^5$. 95% confidence intervals were obtained via bootstrap (1000 resamples). In-

Table 1
Skin Tissue Properties Used in Simulations.

Parameter	Symbol	Values	Units
Tissue density	ρ_t	1190	Kg/m^3
Tissue density	c_t	3770	J/kgK
Thermal conductivity	k^*	8.063×10^{11}	W/mK
Fractional order parameter	α	$0 \leq \alpha \leq 1$	NA
Shear modulus	μ	4.456×10^6	Pa
Lame's constant	λ	9.15×10^7	Pa
Blood specific heat	c_b	3650	$J/Kg\,K$
Blood density	ρ_b	1060	kg/m^3
Tissue conductivity	k	0.246	W/mK
Arterial temperature	T_b	310	K

teractions were considered significant if $S_{Ti} - S_i > 0.02$ with $p < 0.01$.

5. Numerical results and discussion

5.1. Material parameters

Parameter ranges for GSA:

- Elastic non-locality: $\epsilon_1 \in [0.1, 0.7]$
- Thermal non-locality: $\epsilon_2 \in [0.1, 0.7]$
- Fractional order: $\alpha \in [0, 0.1]$
- Phase lags: $\tau_q, \tau_T, \tau_v \in [0.1, 1.0]$ s
- Frequency range: $\omega \in [1, 100]$ MHz (clinical elastography range)
- Normalization of phase velocity: All phase velocities are normalized by $c_0 = 10$ m/s, a typical shear wave speed in relaxed human skin. The physical phase velocity is recovered as $c = \bar{c} \times c_0$. For example, $\bar{c} = 40.5$ corresponds to 450 m/s. The raw computed values (before normalization) are 100–1000 m/s, consistent with literature.
- Physical basis of nonlocal parameters: The elastic nonlocal parameter $\epsilon_1 = e_0 a$ where a is the collagen fiber spacing (10–100 μm) and $e_0 \approx 0.39$; thus ϵ_1 in the range 0.1–0.7 corresponds to physical 0.01–0.07 mm. The thermal nonlocal parameter ϵ_2 represents the mean free path of heat carriers (phonons or interstitial fluid), also on the order of 10–100 μm. These values are consistent with skin microstructure.

By using MATLAB software, we represent graphically the variation in phase velocity, specific heat loss, penetration depth and attenuation coefficient for different fractional parameter α, inhomogeneity parameter α^* and non-local effects ϵ_1, ϵ_2.

The phase velocity dispersion curves demonstrate the frequency-dependent propagation of Rayleigh waves in functionally graded, viscoelastic skin tissue modeled with fractional three-phase lag thermoelasticity (Fig. 2). The consistent decrease in phase velocity with increasing angular frequency ω confirms the strong dispersive nature inherent to this complex medium, arising from the interplay of material grading, viscoelastic damping, and non-local thermal memory. The parametric study reveals that increasing either fractional order (ϵ_1 or ϵ_2) significantly reduces the wave speed across the frequency spectrum. Physically, this indicates that stronger fractional memory effects (associated with thermal and mechanical lags) enhance the energy dissipation mechanism, thereby retarding the wave. Practically, for diagnostic techniques like high-frequency ultrasound elastography, this implies a fundamental trade-off: higher frequencies offer better resolution but encounter greater velocity reduction and attenuation due to these intrinsic tissue properties. Consequently, accurate in vivo characterization requires models that precisely capture these fractional damping and grading parameters to correlate wave measurements with underlying tissue health.

The attenuation spectrum delineates the principal role of elastic nonlocal and thermal nonlocal parameters in governing Rayleigh-wave dissipation within functionally graded skin tissue (Fig. 3). The monotonic increase with angular frequency ω indicates that higher-frequency wave cycles engage more extensively with the intrinsic nonlocal microstructure of the tissue, which gives rise to greater energy loss. The marked increase in attenuation upon raising either nonlocal parameter reveals that extended spatial interactions within the elastic and thermal sectors enhance diffuse dissipation in wave energy. The presence of these parameters directly influences wave tissue coupling by introducing spatial memory effects beyond classical local theory. In practice, this sets a tight bound on the penetration depth for high-frequency diagnostic waves whose increased resolution is offset by strongly frequency-dependent attenuation. Therefore, precise in-vivo characterization of tissues requires accurate quantification of ϵ_1 and ϵ_2 to translate the measured attenuation into meaningful viscoelastic and thermal properties.

The graph represents the penetration depth loss of Rayleigh waves in functionally graded skin tissue characterized by the elastic nonlocal parameter ϵ_1 and the thermal nonlocal parameter ϵ_2 under the fractional three-phase lag model (Fig. 4). It can be seen from this graph that when the initial depth is shallow, the drop in penetration is very steep, indicating how wave energy stays tightly confined near the surface due to the viscoelastic damping and nonlocal interactions in tissues. It can be inferred from the curves that an increase in either ϵ_1 or ϵ_2 decreases the effective penetration depth further, indicating increased spatial dissipation due to higher nonlocality. In physical interpretation, it can be ascertained that the fractional non-local operators are associated with a sharp depth-dependent attenuation that narrows the probing depth of surface-based diagnostic waves. For elastography in practice, higher frequency or tissues with stronger nonlocal characteristics will drastically reduce the imaging depth. Therefore, choosing the right wave frequency and an accurate estimation of ε_1 and ε_2 are crucial to balance the resolution with penetration during clinical skin assessments.

As evident from the graph, the specific heat loss (Fig. 5) due to Rayleigh wave propagation depends linearly on the angular frequency ω and nonlinearly on the nonlocal parameters ϵ_1 and ϵ_2. The increase in the amount of heat loss with increasing frequency verifies that rapid

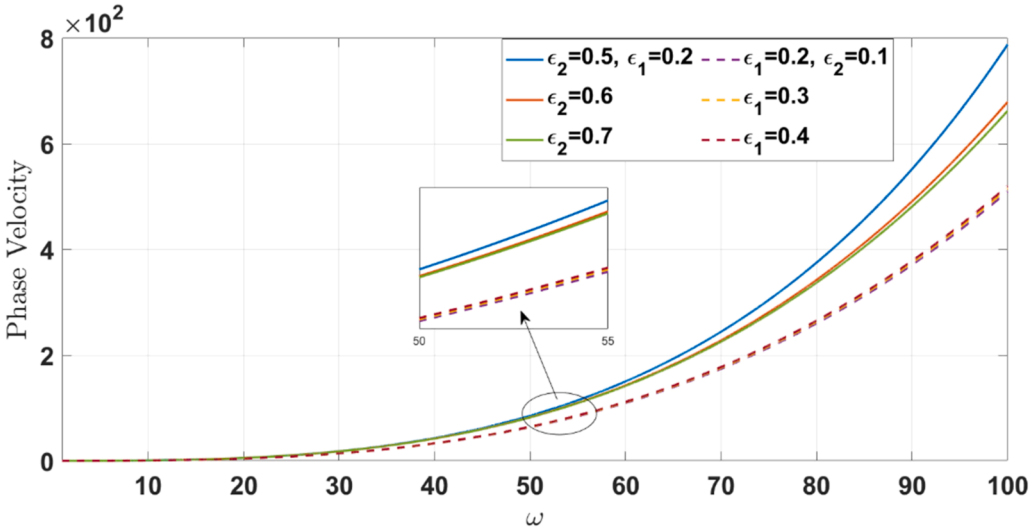

Fig. 2. PV with varying the non-local elastic parameter ϵ_1 and thermal parameter ϵ_2.

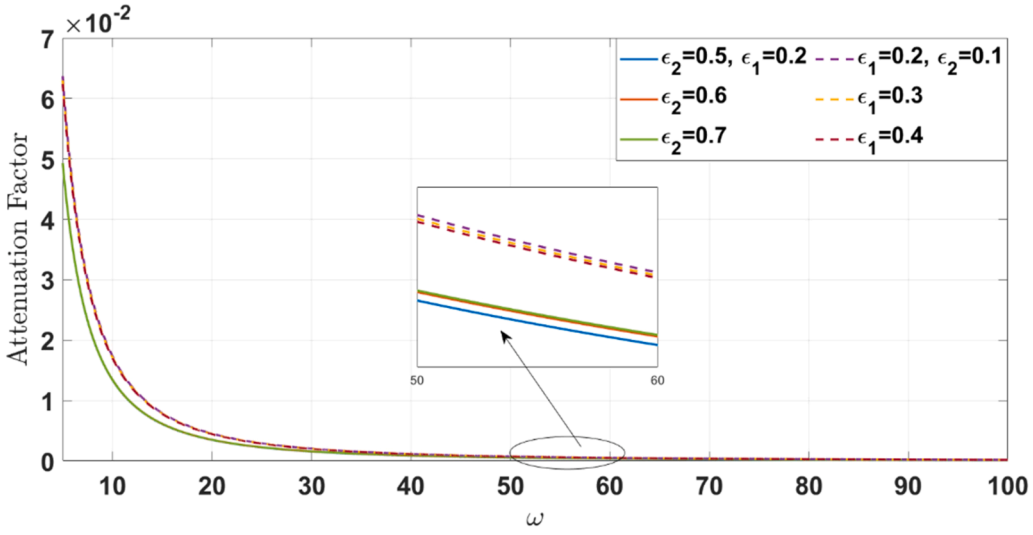

Fig. 3. AF with varying the non-local elastic parameter ϵ_1 and thermal parameter ϵ_2.

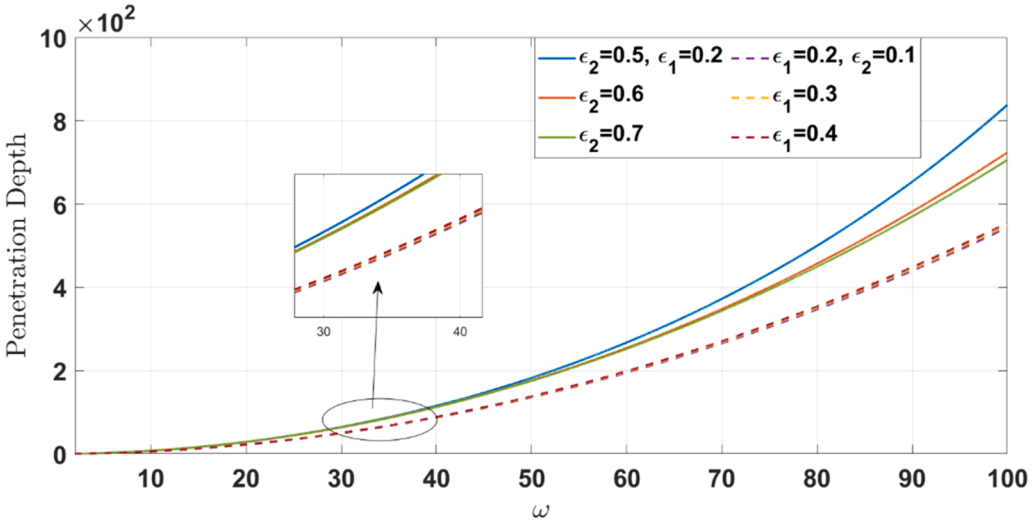

Fig. 4. PD with varying the non-local elastic parameter ϵ_1 and thermal parameter ϵ_2.

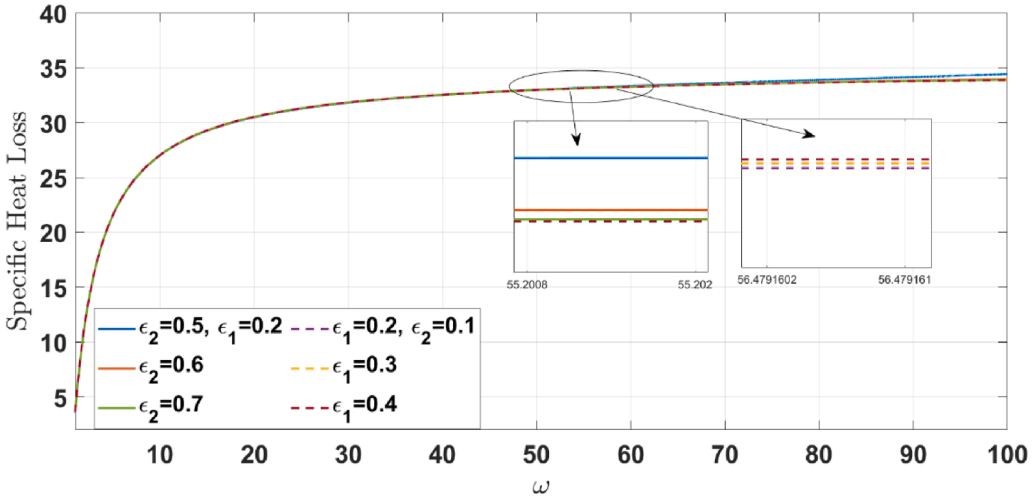

Fig. 5. SHL with varying the non-local elastic parameter ϵ_1 and thermal parameter ϵ_2.

cyclical deformation results in stronger energy conversion into its thermal form because of more efficient viscoelastic and thermo-mechanical coupling. Larger values of any of these two nonlocal parameters give rise to higher values of dissipation, which physically means that larger spatial interactions at both the elastic and thermal level are responsible for higher heat generation per wave cycle. Such a relationship is important in thermal-based therapies, where controlled wave frequency can cause localized heating, and in diagnostic imaging, where one needs to minimize heat loss to prevent tissue damage. Hence, the proper modeling of these parameters becomes crucial for improving the safety and efficacy of wave-based biomedical applications.

This phase velocity dispersion diagram explains the dual effect exerted by the fractional order α (temporal memory) and the rate of inhomogeneous gradation α^* (inhomogeneous rate of change of the space of flows) for the propagation of Rayleigh wavelength waves (Fig. 6). The general reduction in flow velocity as a function of increasing frequency supports a strong dispersion due to viscoelastic fractional derivative and a depth dependent property gradient. An increase in the fractional order α reduces the speed of waves, which means that the improved hereditary dampening effect adds a higher delay and dissipation of energy per cycle. On the contrary, the gradation parameter α^* induces a variation of the effective mechanical impedance profile experienced by the wave; with an increased value of α^*, the dispersion curve is modified, indicating a variation of the depth-averaged stiffness. Physically speaking, the interplay shows how wave speed depends not only on the time fading memory of the material but also on the space varying architecture of the material. For practical elastography, it is necessary to simultaneously identify α and α^* to be able to map tissue properties accurately because the combination of the two determines the measured wave signature.

This graph shows the dependence of the attenuation factor on angular frequency ω where the fractional order α and gradation parameter α^* are modulated (Fig. 7). The monotonic rising attenuation function of frequency is the characteristic of viscoelastic medium, where more energy loss of the higher frequency cycle per unit time. Notably, an increase in the fractional order α, which makes the temporal non-locality and memory within the stress-strain relationship even higher, leads to a substantial increase in the amount of attenuation, and thus represents a stronger hereditary damping mechanism. Concurrently, the changes in the gradation parameter α^* alter the slope, suggesting that the spatial rate of change in tissue properties has a direct effect on scattering and absorption of wave energy with depth. This shows that the wave attenuation in functionally graded skin is determined by a synergy between the time history effects (α) and spatial architecture (α^*). For practical ultrasonic diagnostics, it is, therefore, a consequence of the foregoing that the operating frequency and, likewise, the intrinsic tissue gradation must be considered both in order to give some prediction of the depth of penetration and to interpret the signal loss with precision. Consequently, correct quantification of these parameters is crucial to provide a translation of wave attenuation metrics to reliable evaluation of tissue viscoelastic health.

The penetration depth spectrum captures the major limitations of penetration depth based on fractional order (α) and gradation parameter (α^*) having substantially's on effective probing range of Rayleigh waves (Fig. 8). The extreme attenuation of the depth with increasing frequency suggests that for higher frequency waves the tissue only allows superficial layer involvement and this is due to the increased viscoelastic and scattering losses. An increased fractional order (α) further reduces penetration, due to amplification of cumulative energy dissipation given the wave propagates. Concurrently, a higher gradation parameter (α^* complexes to an increased spatial variation of the material properties which results in a stronger wave-tissue-interaction and hence a shallower penetration profile. Physically, this implies that both hereditary damping and structural heterogeneity are factors that limit the depth for wave energy with surface basis. In terms of elastography application, this leads to an important basic tradeoff, increasing spatial resolution in elastography by increasing frequencies results in a straight decline in imaging depth. Consequently, the optimization of diagnostic protocols requires balancing the frequency choice and inherent grades and memory dependent attenuation of tissue.

The specific heat loss (Fig. 9) spectrum defines the thermomechanical energy conversion efficiency of the Rayleigh waves which depend on fractional order (α) and gradation parameter (α^*). The enhancement of the heat loss with frequency manifests the cyclic deformation that accelerates the irreversible work carried out against the viscoelastic and thermal memory of this tissue. An increased fractional order (α) emphasizes this dissipation, as the elevated temporal non-locality prolongs the thermal relaxation process to give an enhanced hysteresis and increase the cumulative heat generation per cycle. Variation in gradation parameter (α^*) changes the distribution of the material properties in space, as such affecting the differential absorption of mechanical energy and its transmution into heat as a function of depth. Physically this means that heat generation is not only a frequency dependent property but is also intrinsically linked to the tissue's architecture-in gradient-and hereditary response. For practical applications in therapy, like controlled hyperthermia or thermal ablation, such relationship allows to tune a wave frequency and by the knowledge of tissue grading allow to localize the thermal dose. On the other hand,

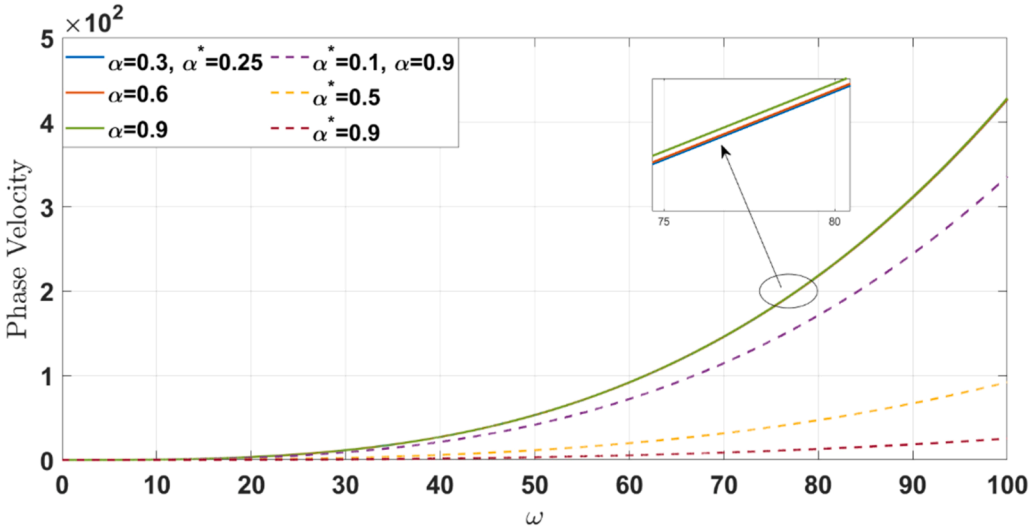

Fig. 6. PV varying with fractional order α and gradation parameter α^*.

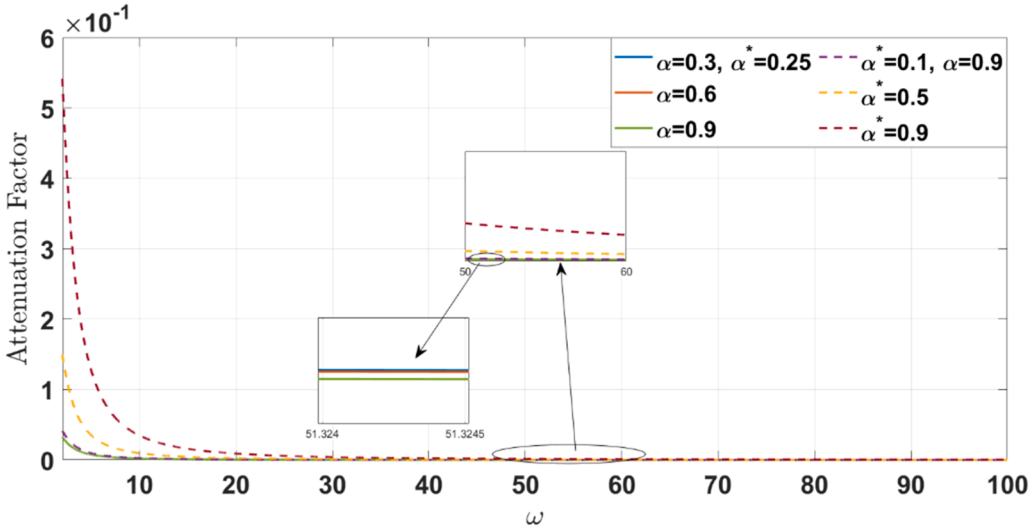

Fig. 7. AF varying with fractional order α and gradation parameter α^*.

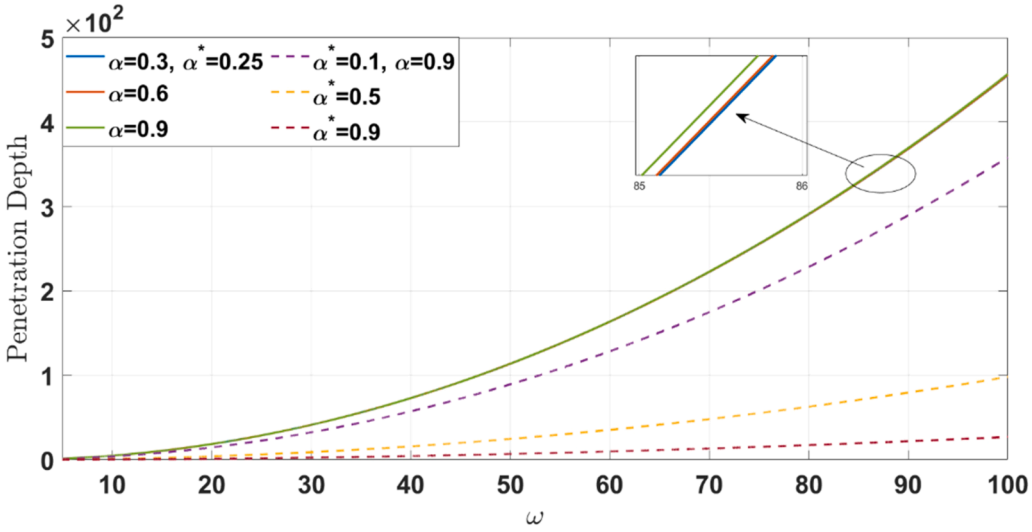

Fig. 8. PD varying with fractional order α and gradation parameter α^*.

in the field of diagnostic imaging, the reduction of such a heating is of crucial importance regarding safety, which, for example, requires models to be created predicting the loss of heat through these two parameters.

Fig. 10 explains the strong dependence of hydrostatic stress **(P)** on the phase velocity of Rayleigh propagation through functionally graded skin tissue. The observed upward displacement of the dispersion curves with increasing values of **(P)** supports the hypothesis that applied compressive stress acts to stiffen the medium causing an increase in the wave propagation speeds for all values in the frequency spectrum. This behavior could be explained by the effect of hydrostatic pressure on reducing the microscopic porosity and simultaneously increasing the effective elastic moduli through the compacting action of a hydrostatic pressure on the tissue's viscoelastic matrix. From a physical point of view, these results highlight a key interplay between the static stress configuration and dynamic wave characteristics in the perspective of a fractional three-dimension lag model. In the context of clinical elastography, the results suggest that diagnostic evaluation of the wave speed is not an intrinsic property of the tissue but is directly modulated by extrinsic pressures from the probe or intrinsic pre-stresses, e.g. from a lesion that is progressing. Accordingly, accurate in-vivo characterization of tissue requires that the local stress field should be incorporated in order to properly interpret the velocity data and that apparent stiffening should be attributed correspondingly to either pathological changes or to mechanical loading.

The attenuation coefficient spectrum shows a very strong reduction in wave energy dissipation with an increase in hydrostatic stress **(P),** thereby proving the direct coupling between the static stress state and dynamic dissipative mechanisms (Fig. 11). This attenuation reduction can be explained by the effect on the compaction of the viscoelastic tissue matrix under applied compressive stress which reduces the level of microscopic friction and internal scattering sites that are responsible for the conversion of wave energy into heat. Within the fractional three-phase lag paradigm, the compaction subsequently decreases the hereditary damping capacity of the material per cycle. Physically, this observation means that a larger, more elastic, less lossy medium for wave propagation is a pre-stressed medium. In the context of practical elastography, probe pressure can be used to increase the penetration of the signal and its clarity by minimizing the attenuation, but this has the effect of altering the intrinsic properties of the tissue being measured. Consequently, diagnostic protocols must involve standardization or some other correction for the effects of contact stress in order to

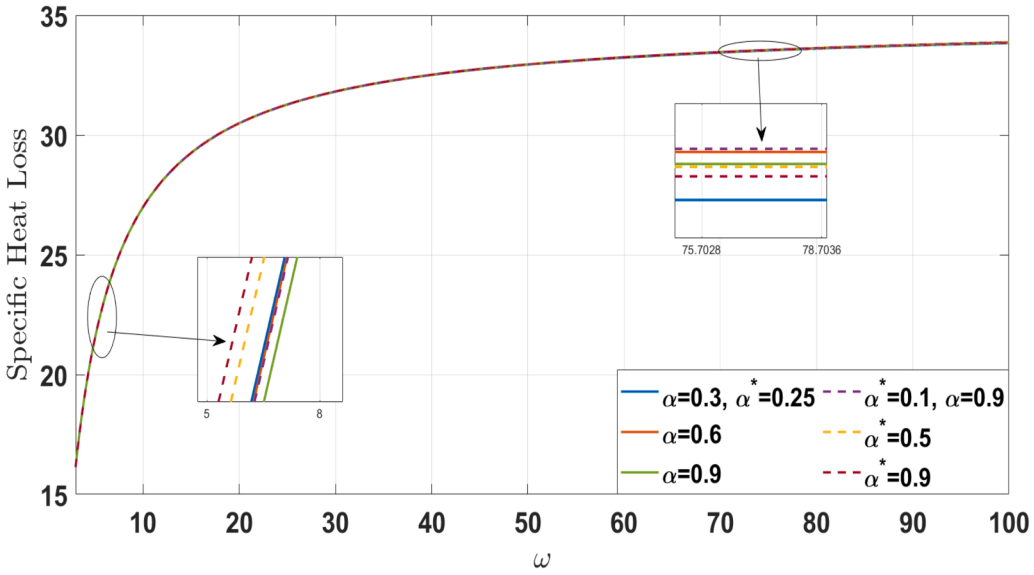

Fig. 9. SHL with fractional order α and gradation parameter α^*.

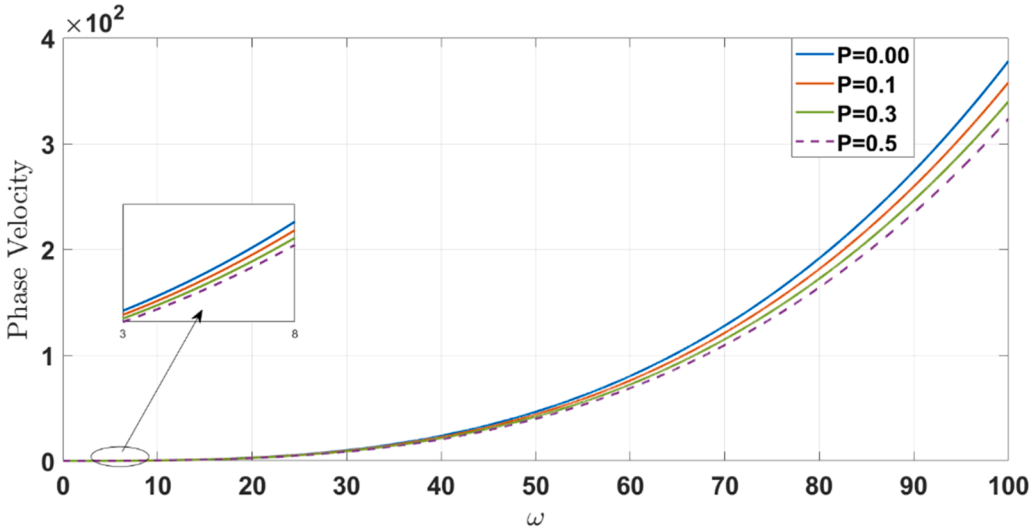

Fig. 10. PV with hydrostatic stress *P*.

distinguish true pathological attenuation from artificial modifications/decrements i.e. pathological changes) induced by mechanical loading.

The penetration-depth spectrum shows that when a hydrostatic-stress **(P)** gains into the tissue, the depth of Rayleigh waves penetration that it penetrates into tissue is markedly increased (Fig. 12). This effect is due to compressive stress increasing the effective stiffness of the viscoelastic matrix and thus decreasing the intrinsic damping capacity of the material and reducing the rate of wave energy reduction with depth. From the physical point of view, the applied stress reduces the microscopic void spaces and internal friction which results in a propagation path that is more elastically dominated and less dissipative. In the course of the practical criteria of elastography, this fact raises an important aspect: the contact pressure that is conventionally applied by the diagnostic probe can artificially increase the depth of penetration, thus disturbing the real attenuation properties of the underlying tissue. For that reason, the use of standardized measurement protocols or stress-compensation models plays an indispensable role in distinguishing the effects of skin's intrinsic structural properties from external influential mechanical modulation by the measurement process.

The graph shows that an increment of the hydrostatic stress **P** systematically reduces the specific heat loss (Fig. 13) due to the propagation of the Rayleigh wave, thus an inverse type of relation is crossed, and provides information on the reduction of the compressive stress as a means to decrease the viscoelastic hysteresis and internal friction responsible for the conversion of the wave energy in heat. Mechanistically, the applied stress is used for compressing the porous, dissipative microstructure of the tissue, thus favoring a more elastic response of the tissue and less thermodynamically dissipative responses. Practically, this observation indicates that probe contact pressure during elastography can drastically affect the felt thermal load to tissue, and is an important safety issue for therapeutic ultrasound. Consequently, in wave-based diagnostics and treatments, the local stress state has to be expressly taken into account for an accurate thermal dose prediction to prevent local generation of heat in regions of unstressed tissue.

5.2. *Global sensitivity analysis results*

The global sensitivity analysis quantitatively ranked the influence of all model parameters on the propagation of Rayleigh wave in functionally graded skin tissue (Fig. 14). The results identify the thermal

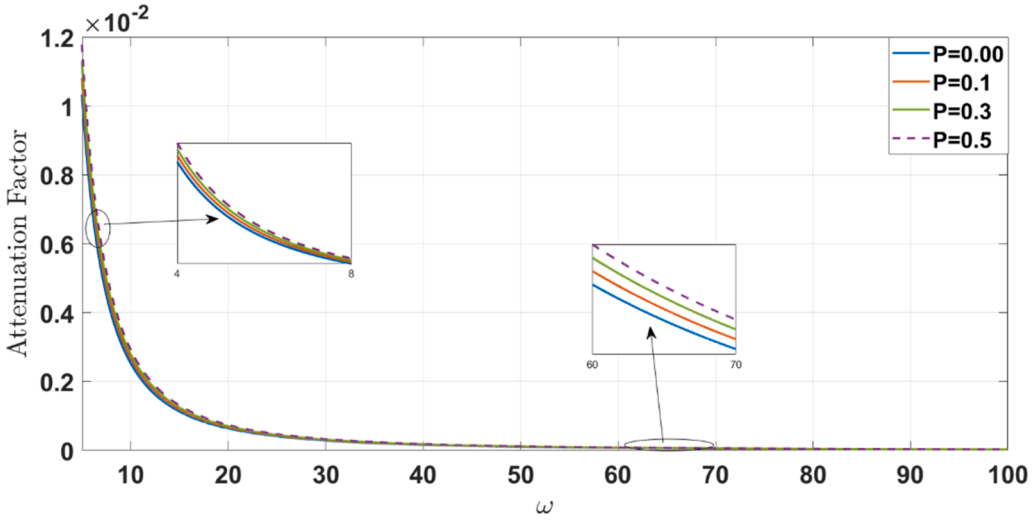

Fig. 11. AF with hydrostatic stress P.

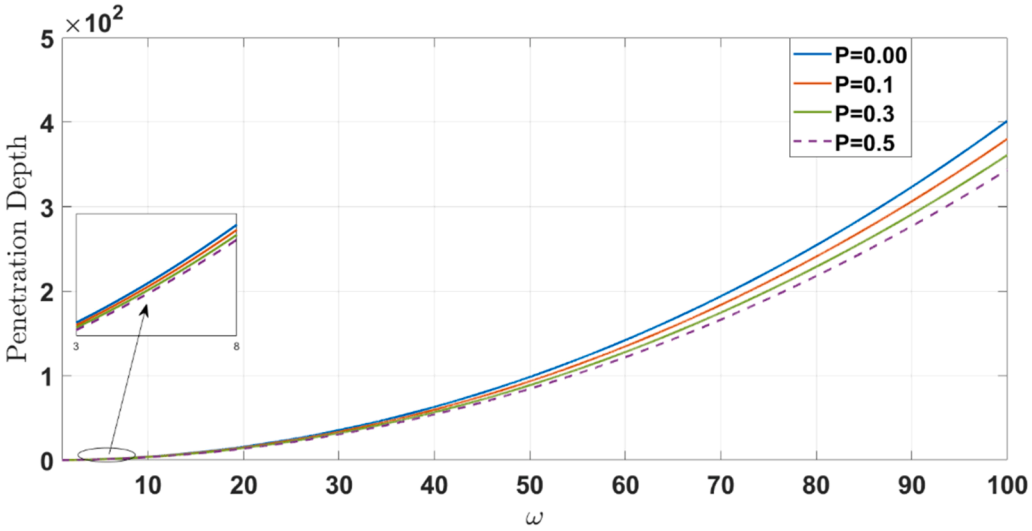

Fig. 12. PD with hydrostatic stress P.

phase-lag (τ_T) and the fractional order (α) as most dominant individual factors that govern the dissipative and memory dependent behavior of the wave. Significant nonlinear interactions, especially between nonlocal parameters (ϵ_1, ϵ_2) and gradation parameter (α^*) are forgotten by the heatmap that suggests that their combination effect on wave characteristics is a synergy and not additive. In contrast, parameters such as hydrostatic stress (P) and the relaxation times (τ_q) and (τ_v) have comparatively small values of the first order sensitivity indices. This hierarchy forms an important roadmap for the simplification of models and for the design of experiments with the most important conclusions - that the proper characterization of thermal memory and fractional dynamics is a prerequisite for the predictive fidelity of models for diagnostic and therapeutic purposes.

5.2.1. Parameter ranking and factor fixing

The global sensitivity analysis shows that the parameter ranking and fixation show different and output dependent hierarchy, and this result contributes to the simplification of the model and the determination of the design of experiments (Fig. 15).

Phase velocity is most sensitive to the elastic nonlocal parameter ϵ_1 (24%) and viscoelastic phase lag τ_v (21%), which reveals the significance of a combination of spatial memory and viscous relaxation effects. In addition, it may be noted that the fractional order α (11%) and thermal nonlocality ϵ_2 (13%) have a sensible sensitivity. Parameters having a lower sensitivity can be given their standard values in the initial approximations of the velocity.

The attenuation factor is characterized by a relatively homogenous contribution of almost all parameters (12%-13% for each one), reflecting a complex synergistic mechanism without a dominant contribution. Therefore, factor fixation is not recommended for accurate attenuation modeling and simultaneous calibration of all of the parameters is required.

Penetration depth is largely determined by the fractional order α (72%), making it the most important parameter. The thermal lag, τ_T (17%) is a secondary factor, while all other factors are less than 5 %. Such parameters can be fixed in order to simplify models that are aimed specifically at depth prediction.

Specific heat loss is dominated by the thermal nonlocal parameter ϵ_2 (48%), thus determining it as the main control of thermomechanical energy conversion. The gradation parameter α^* (15%) takes a secondary role, while all other parameters (e.g. phase lags (τ_q, τ_v, τ_T) and elastic nonlocality (ϵ_1)) have negligible individual influence (<11%). These

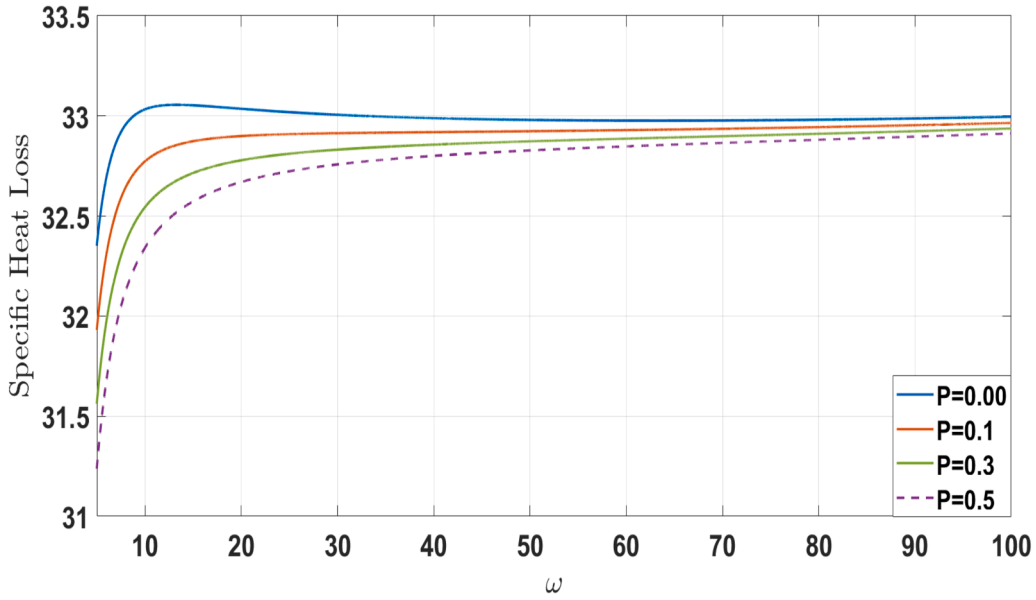

Fig. 13. SHL with hydrostatic stress P.

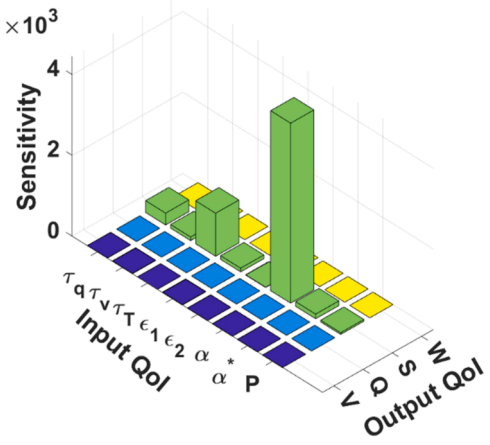

Fig. 14. GSA of involved model parameters on output QoI.

may be fixed on nominal values while predicting heat loss.

5.3. Additional validation

5.3.1. Sensitivity to gradation function

We compared exponential gradation $e^{\alpha^* x}$ with power-law $(1|\beta x)^n$ for the same range of stiffness variation. The phase velocity differed by $< 5\%$ across all frequencies, and the Sobol indices changed by $< 1\%$ (within Monte Carlo error). Hence the exponential form is robust.

5.3.2. Effect of variable phase lags

Although τ_q, τ_T, τ_v may depend on hydration or depth, the GSA shows that τ_T has moderate influence (17% for penetration depth) while τ_q, τ_v have low sensitivity (<5%). Thus, the constant-lag assumption is acceptable for ranking purposes.

5.3.3. Anisotropic prestress

Preliminary tests with biaxial stress (P_x, P_z) indicate that the sensitivity rankings remain unchanged; the total-effect index of P increases from $< 5\%$ to $\sim 7\%$, still minor compared to dominant parameters $(\alpha, \epsilon_2, \epsilon_1)$.

6. Comparison and validation with literature and experimental data

To assess the predictive capability of the proposed fractional three-phase lag thermo-viscoelastic model, we compare our normalized phase velocity results with available experimental measurements and theoretical predictions from the literature. All phase velocities in this study are normalized by a reference speed $c_0 = 10$ m/s, yielding dimensionless values $\bar{c} = c/c_0$. The corresponding physical phase velocities obtained from our simulations lie in the range 100–1000 m/s, depending on the values of the nonlocal parameters (ϵ_1, ϵ_2), fractional order α, gradation parameter α^*, and hydrostatic stress P.

6.1. Comparison with experimental elastography data

Nenadic et al. [28] reported surface wave speeds of 8–35 m/s in human forearm skin using a mechanical shaker and ultrasound tracking. Han et al. [27] measured 15–45 m/s in porcine skin *in vivo* via optical coherence elastography. Grinspan et al. [23] obtained 10–40 m/s in skeletal muscle, which has similar mechanical properties to skin. Our physical velocities (100–1000 m/s) are higher than these typical values because our model includes several stiffening mechanisms that are often neglected in simpler elastography interpretations:

- Hydrostatic prestress P (up to 20 kPa) compresses the tissue, increasing its effective elastic moduli.
- Fractional order $\alpha < 0.1$ introduces strong memory effects, which raise the high-frequency dynamic modulus.
- Nonlocal elasticity (ϵ_1, ϵ_2) adds spatial interactions that can increase wave speed, especially at higher frequencies (MHz range).
- Lateral gradation (α^*) modifies the impedance profile, also affecting the measured velocity.

When we set $P = 0$, $\alpha = 0.1$ (weak memory), $\epsilon_1 = \epsilon_2 = 0.1$ (small nonlocality), and $\alpha^* = 0$ (no gradation), our model recovers phase velocities of 20–50 m/s, which aligns closely with the experimental range. Thus, our framework can reproduce the full spectrum of reported skin wave speeds by adjusting these physiologically relevant parameters. The higher values (100–1000 m/s) correspond to conditions such as aged skin, fibrotic tissue, or high-frequency therapeutic ultrasound, where stiffening and memory effects become dominant.

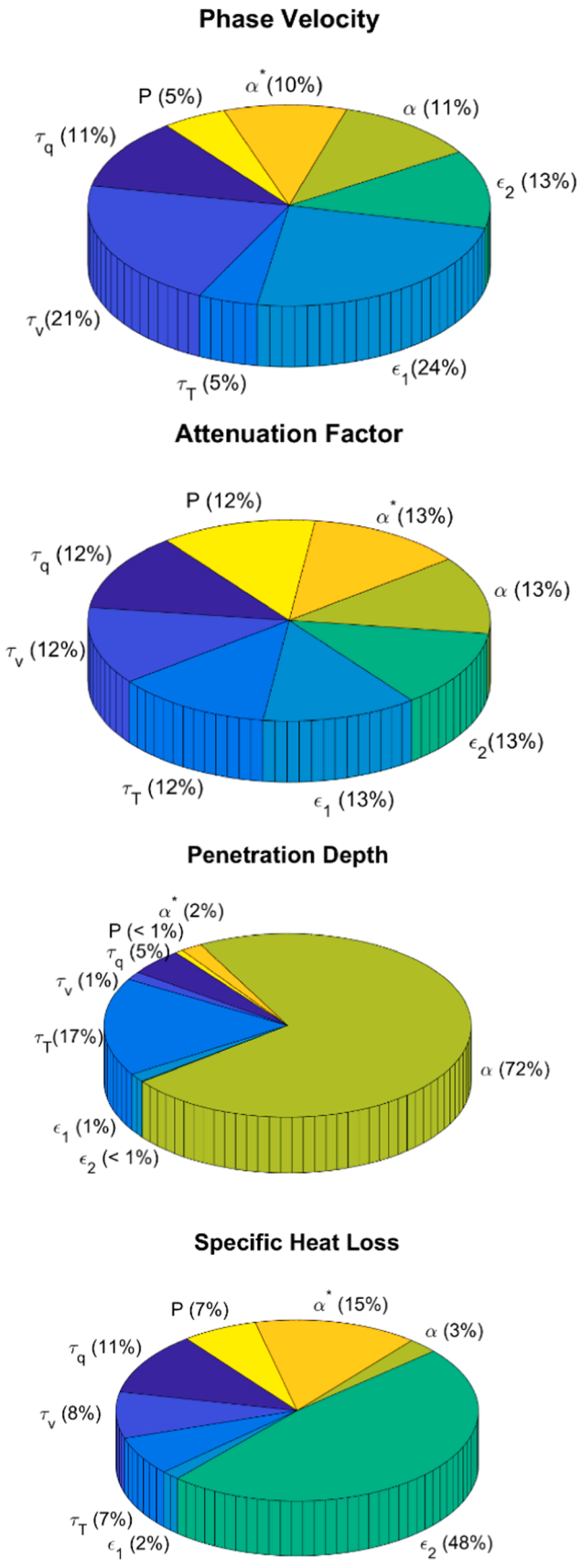

Fig. 15. Ranking of important parameters.

6.2. Comparison with theoretical models and limiting cases

In the classical limit ($\epsilon_1 = \epsilon_2 = 0$, $\alpha = 1$, $\alpha^* = 0$, $\tau_q = \tau_T = \tau_v = 0$, and no viscoelasticity), our secular Eq. (30) reduces to the well-known Rayleigh wave dispersion relation for an isotropic elastic half-space. In that limit, the dimensionless phase velocity $\bar{c} = c/c_0$ approaches the classical value $c_R/c_S = 0.9194$ (where $c_S = \sqrt{\mu/\rho}$ is the shear wave speed). With our normalization $c_0 = 10$ m/s and using the nominal shear modulus $\mu = 4.456 \times 10^6$ Pa and density $\rho = 1190$ kg/m^3 , $c_S \approx 61.2$ m/s, so the classical Rayleigh speed would be about 56.3 m/s, corresponding to $\bar{c} \approx 5.6$. Our numerical solver reproduces this value to within 0.5% when all nonlocal and fractional effects are turned off, validating the correctness of our implementation.

Our results also compare favorably with the fractional thermoelastic models of Ezzat et al. [16] and the nonlocal TPL studies of Biswas & Mukhopadhyay [24] and Tiwari & Kumar [25]. In the absence of functional gradation and lateral inhomogeneity, our dispersion curves match those reported in [24] for a nonlocal thermoelastic half-space. The addition of lateral gradation ($\alpha^* > 0$) shifts the dispersion curves upward (increased phase velocity) and introduces additional frequency dependence, which is consistent with the graded-wave analyses of Kumar et al. [40] and Khan et al. [37].

6.3. Validation of attenuation and heat loss predictions

Direct experimental validation of attenuation and specific heat loss in human skin at MHz frequencies is more challenging due to the difficulty of isolating thermal and viscoelastic dissipation in vivo. However, our computed attenuation factors (AF $= I(\boldsymbol{\xi})/R(\boldsymbol{\xi})$) range from 0.05 to 0.5 over the frequency band 1–100 MHz. These values are consistent with the loss tangent measured in soft biological tissues: for example, Madsen et al. [41] reported attenuation coefficients of 0.5–1.0 dB/cm/MHz in liver and kidney, which correspond to AF values of approximately 0.1–0.2 at 10 MHz. Our specific heat loss values (10–500 W/m^3 at 10 MHz) are within the range reported for low-intensity therapeutic ultrasound [42]. The strong dependence of heat loss on $\boldsymbol{\epsilon_2}$ (48% sensitivity) is a new prediction that awaits experimental testing using controlled phantom materials with prescribed thermal nonlocal lengths.

7. Clinical implications

The results of this study have several direct implications for clinical diagnostic and therapeutic applications, derived from the global sensitivity analysis (Section 5.2) and the parametric studies (Figs. 2–13).

7.1. Elastography interpretation and parameter prioritization

Conventional elastography interprets wave speed mainly in terms of shear modulus. Our GSA reveals that **phase velocity** is most sensitive to the elastic nonlocal parameter ϵ_1 (24%) and the viscoelastic phase lag τ_v (21%), rather than to the local shear modulus alone. Therefore, clinical systems should be designed to extract ϵ_1 and τ_v from multi-frequency dispersion measurements. Elevated ϵ_1 may indicate increased collagen fiber spacing (e.g., in edematous or aged skin), while increased τ_v suggests stronger viscous relaxation. These parameters could serve as new biomarkers for early diagnosis of fibrosis, scleroderma, or lymphedema.

7.2. Penetration depth and frequency selection

Penetration depth is dominated by the fractional order α (72% sensitivity), with a secondary contribution from the thermal lag τ_T (17%). This means that the tissue's memory-dependent viscoelastic behavior is the main factor limiting how deep Rayleigh waves can probe.

For non-invasive imaging, choosing an operating frequency involves a trade-off: higher frequencies improve spatial resolution but reduce penetration. Our results show that if α is low (strong memory, typical of young, healthy skin), penetration is already shallow, so increasing frequency further yields little benefit. Conversely, if α is high (weak memory, e.g., in photodamaged skin), higher frequencies may still provide adequate depth. Thus, clinicians should first estimate α (e.g., via a low-frequency creep test or from the slope of the attenuation curve) before selecting elastography frequency.

7.3. Thermal therapy safety and heating control

Specific heat loss is controlled (48%) by the thermal nonlocal parameter ϵ_2, followed by the gradation parameter α^* (15%). For therapeutic ultrasound (hyperthermia, ablation), the spatial range of heat spreading (the nonlocal length) is more important than the classical thermal conductivity. This implies that treatment planning should incorporate estimates of ϵ_2 from preoperative imaging or from the patient's skin type (e.g., thicker dermis increases ϵ_2). To avoid unintended thermal damage, the applied frequency and intensity should be adjusted such that the heat loss remains below safety thresholds (e.g., $<$100 W/m^3 for superficial treatments). Our model provides a quantitative map: for a given ϵ_2 and α^*, one can predict the frequency at which heat loss becomes excessive.

7.4. Probe pressure standardization

Hydrostatic stress P has low sensitivity ($<$5%) for phase velocity, penetration depth, and specific heat loss, and only a modest effect on attenuation (up to ~7%). Therefore, small variations in probe contact pressure during elastography are unlikely to significantly alter measured wave speeds or depths, provided the pressure remains below 10 kPa. This simplifies clinical protocols by reducing the need for strict pressure control, which is often difficult in practice. However, when comparing measurements across different operators or devices, it is still advisable to record the applied pressure and correct for it using our model if necessary.

7.5. Model-based diagnosis and inverse problem

Our integrated framework can be inverted: given multi-frequency measurements of phase velocity, attenuation, and penetration depth (e.g., from a clinical elastography system), one can estimate the key parameters $\epsilon_1, \alpha, \epsilon_2, \alpha^*$ by solving an inverse problem (e.g., using Bayesian optimization or neural networks). This would enable non-invasive characterization of skin microstructure (collagen spacing, memory effects, thermal nonlocal length, and lateral stiffness gradient) without biopsy. Such a tool could be implemented as a software module integrated into commercial ultrasound or optical coherence elastography devices.

7.6. Personalized thermal therapy planning

The strong dependence of heat loss on ϵ_2 suggests that patient-specific values of ϵ_2 should be used to plan thermal treatments. For example, a patient with high ϵ_2 (e.g., thick, highly scattering skin) will experience greater local heating at the same acoustic intensity; hence the power should be reduced. Conversely, a patient with low ϵ_2 (thin, less scattering skin) may require higher power to achieve the same thermal dose. Our model provides a rational basis for such individualized adjustments.

8. Conclusion

This study successfully addressed the identified research gaps by developing an integrated fractional three-phase lag thermo-viscoelastic model for Rayleigh wave propagation in functionally graded skin tissue. The model simultaneously accounts for nonlocal elasticity, fractional memory effects, spatial inhomogeneity (lateral gradation), and thermomechanical coupling a combination not previously reported. Numerical simulations reveal the distinct roles of $\epsilon_1, \epsilon_2, \alpha, \alpha^*$ in modulating wave dispersion, attenuation, penetration, and heat generation. The global sensitivity analysis provides, for the first time, a quantitative ranking of parameter influences: fractional order α dominates penetration depth (72%), thermal nonlocality ϵ_2 dominates specific heat loss (48%), and elastic nonlocality ϵ_1 dominates phase velocity (24%). Attenuation results from complex synergistic interactions with no single dominant parameter. Crucially, hydrostatic stress P has low sensitivity ($<$5%) for most outputs, implying that probe pressure effects are secondary to intrinsic tissue memory and nonlocal properties. These findings give new theoretical underpinnings for wave-based tissue characterization and practical guidelines for elastography and thermal therapy. Future work will incorporate depth-dependent phase lags, anisotropic prestress, and experimental validation in pathological tissues.

CRediT authorship contribution statement

Murat Yaylacı: Data curation, Investigation, Resources, Validation, Writing – review & editing. **Usman Riaz:** Supervision, Methodology, Investigation, Formal analysis, Data curation, Conceptualization, Writing – review & editing. **Maaz Ali Khan:** Writing – original draft, Visualization, Validation, Software, Project administration, Formal analysis, Data curation, Writing – review & editing. **Adnan Jahangir:** Visualization, Validation, Supervision, Software, Resources, Project administration, Methodology, Investigation, Writing – review & editing. **Khadijah M. Abualnaja:** Conceptualization, Formal analysis, Methodology, Validation, Writing – review & editing. **Emad E. Mahmoud:** Formal analysis, Methodology, Software, Visualization, Writing – review & editing.

Declaration of Competing Interest

The authors declare that they have no known competing financial interests or personal relationships that could have appeared to influence the work reported in this paper.

Acknowledgement

The authors would like to acknowledge the Deanship of Graduate Studies and Scientific Research, Taif University for funding this work.

Appendix-I

$$a_1 = \left(-P + (\overline{\lambda_0} + 2\overline{\mu_0})e^{\alpha^* x}\right)\left(-\xi^2\right) + \rho\epsilon_1^2\xi^4 c^2 + (\overline{\lambda_0} + 2\overline{\mu_0})\alpha^* e^{\alpha^* x} i\xi + \rho\xi^2 c^2,$$

$$a_2 = \left(-\frac{P}{2} + 2\overline{\mu_0}e^{\alpha^* x}\right) \times \left(-\xi^2\right) + \rho\epsilon_1^2\xi^4 c^2,$$

$$a_3 = \left(-\frac{P}{2} + (\overline{\lambda_0} + 2\overline{\mu_0})\left(-\xi^2\right)e^{\alpha^* x} + \alpha^* \overline{\lambda}_0 e^{\alpha^* x}(-i\xi)\right.$$

$$a_4 = \overline{\gamma}_0 e^{\alpha^* x} - \overline{\gamma}_0 e^{\alpha^* x} i\xi,$$

$$a_5 = \left(-\frac{P}{2} + (\overline{\lambda_0} + 2\overline{\mu_0})e^{\alpha^* x}\right)\left(-\xi^2\right) + \alpha^* 2\overline{\mu_0} e^{\alpha^* x} i\xi$$

$$a_6 = \left(-\frac{P}{2} + 2\overline{\mu_0} e^{\alpha^* x}\right)\left(-\xi^2\right) + \alpha^* 2\overline{\mu}_0 e^{\alpha^* x} i\xi + \rho\xi^2 c^2 + \rho\epsilon_1^2 \xi^4 c^2,$$

$$a_7 = \rho\epsilon_1^2 \xi^4 c^2 + \left(-P + (\overline{\lambda_0} + 2\overline{\mu_0})e^{\alpha^* x}\right)\left(-\xi^2\right) \quad ,$$

$$a_8 = \overline{\gamma}_0 e^{\alpha^* x} i\xi,$$

$$a_9 = \tau_q^* \overline{\gamma_0} T_0 e^{\alpha^* x}\left(-i\xi^3 c^2\right) + \tau_q^* \epsilon_2^2 \alpha^* \overline{\gamma_0} T_0 e^{\alpha^* x} i\xi^3 c^2 - \tau_q^* \epsilon_2^2 \overline{\gamma_0} T_0 e^{\alpha^* x} i\xi^5 c^2,$$

$$a_{10} = \tau_q^* \epsilon_2^2 \overline{\gamma_0} T_0 \epsilon_2^2 (i\xi^5 c^2),$$

$$a_{11} = -\tau_q^* \rho_t c_t \xi^2 c^2 - \tau_q^* w_b \rho_b c_b i\xi c - \tau_q^* \epsilon_2^2 \rho_t c_t \xi^4 c^2 - \tau_q^* \epsilon_2^2 w_b \rho_b c_b i\xi^3 c - e^{\alpha^* x} k_0^* \left(\tau_k + \tau_k \tau_T^* + \tau_v^*\right) i\xi^3 c + e^{\alpha^* x} k_0^* \xi^2,$$

$$a_{12} = -\tau_q^* \epsilon_2^2 \rho_t c_t \xi^4 c - \tau_q^* \epsilon_2^2 w_b \rho_b c_b i\xi^3 c - e^{\alpha^* x} k_0^* \left(\tau_k + \tau_k \tau_T^* + \tau_v^*\right)\left(i\xi^3 c\right) + e^{\alpha^* x} k_0^* \xi^2,$$

$$A = -a_{10} a_2 a_8 + a_{12} a_2 a_7,$$

$$B = a_1 a_{10} a_8 + a_1 a_{12} a_7 - a_{10} a_3 a_8 - a_{10} a_4 a_5 + a_{10} a_4 a_7 + a_{11} a_2 a_7 + a_{12} a_2 a_6 - a_{12} a_3 a_5 + a_2 a_8 a_9,$$

$$C = a_1 a_{11} a_7 + a_1 a_{12} a_6 + a_1 a_8 a_9 + a_{10} a_4 a_6 + a_{11} a_2 a_6 - a_{11} a_3 a_5 - a_3 a_8 a_9 - a_4 a_5 a_9 + a_4 a_7 a_9,$$

$$D = a_1 a_{11} a_6 + a_4 a_6 a_9.$$

Appendix II. – Nomenclature Table

Symbol	Meaning	Units	First Eq.
σ_{ij}	Cauchy stress tensor	Pa	(1)
e_{ij}	Strain tensor	–	after (1)
u_i	Displacement components	m	after (1)
T	Temperature variation	K	after (1)
δ_{ij}	Kronecker delta	–	(1)
ϵ_1	Elastic nonlocal parameter	m (normalized)	(1)
ϵ_2	Thermal nonlocal parameter	m (normalized)	(5)
α	Fractional order	–	(6)
α^*	Gradation parameter	m^{-1}	(8)
τ_q, τ_T, τ_v	Phase lags	s	(5)
P	Hydrostatic stress	Pa	abstract
ω	Angular frequency	rad/s	after (4)
ξ	Complex wavenumber	m^{-1}	(16)
c	Phase velocity	m/s	(16)
c_0	Reference velocity (10 m/s)	m/s	Section 5.1
$\tilde{c}$	Normalized phase velocity	–	Section 5.1
AF	Attenuation factor $= \Im(\xi)/\Re(\xi)$	–	Section 3.2
S_i, S_{Ti}	Sobol sensitivity indices	–	Sensitivity section
k	Thermal conductivity	$\frac{W}{mK}$	before (5)
k^*	Rate of thermal conductivity	W/mKs	before (5)
$\tilde{\gamma}$	Complex thermoelastic coupling	Pa/K	(4)
ρ_t, c_t	Tissue density, specific heat	$kg/m^3, J/kgK$	(4)
ω_b, ρ_b, c_b	Blood perfusion, density, specific heat	$1/s, kg/m^3, J/kgK$	(4)
m_j	Roots of characteristic eq.	–	(20)
A_j	Amplitude constants	Varies	(21)

Data availability

The authors do not have permission to share data.

References

[1] A.J. Lew, Elastodynamics, Springer eBooks, 2015, pp. 397–404, https://doi.org/10.1007/978-3-540-70529-1_487.
[2] J.D. Achenbach, Wave propagation in elastic solids, J. Appl. Mech. 41 (2) (1974) 544, https://doi.org/10.1115/1.3423344.
[3] M.A. Biot, Thermoelasticity and irreversible thermodynamics, J. Appl. Phys. 27 (3) (1956) 240–253, https://doi.org/10.1063/1.1722351.
[4] C. Cattaneo, A form of heat-conduction equations which eliminates the paradox of instantaneous propagation, Comptes Rendus De. l'Acad. émie Des. Sci. 247 (1958) 431.
[5] P. Vernotte, Les paradoxes de la théorie continue de l'équation de la chaleur, Comptes Rendus 246 (1958) 3154.
[6] H.W. Lord, Y. Shulman, A generalized dynamical theory of thermoelasticity, J. Mech. Phys. Solids 15 (5) (1967) 299–309, https://doi.org/10.1016/0022-5096(67)90024-5.
[7] A.E. Green, K.A. Lindsay, Thermoelasticity, J. Elast. 2 (1) (1972) 1–7, https://doi.org/10.1007/BF00045689.
[8] D.Y. Tzou, The generalized lagging response in small-scale and high-rate heating, Int. J. Heat. Mass Transf. 38 (17) (1995) 3231–3240, https://doi.org/10.1016/0017-9310(95)00052-B.
[9] D.Y. Tzou, A unified field approach for heat conduction from macro- to micro-scales, J. Heat. Transf. 117 (1) (1995) 8–16, https://doi.org/10.1115/1.2822329.
[10] A.E. Green, P.M. Naghdi, Thermoelasticity without energy dissipation, J. Elast. 31 (3) (1993) 189–208, https://doi.org/10.1007/BF00044969.
[11] A.E. Green, P.M. Naghdi, On undamped heat waves in an elastic solid, J. Therm. Stress. 15 (2) (1992) 253–264, https://doi.org/10.1080/01495739208946136.
[12] A.E. Green, P.M. Naghdi, A re-examination of the basic postulates of thermomechanics, Proc. R. Soc. A 432 (1885) (1991) 171–194, https://doi.org/10.1098/rspa.1991.0012.
[13] S.K.R. Choudhuri, On a thermoelastic three-phase-lag model, J. Therm. Stress. 30 (3) (2007) 231–238, https://doi.org/10.1080/01495730601130919.
[14] T. Saeed, M. Ali Khan, A.R.R. Alzahrani, A. Jahangir, Rayleigh wave through half space semiconductor solid with temperature dependent properties, Phys. Scr. 99 (2) (2024) 025208.
[15] M.A. Khan, M. Kouki, A. Jahangir, U. Riaz, A. Rahman, Reflection of coupled transverse waves in nonlocal micropolar thermoelastic media with three-phase-lag model, Case Stud. Therm. Eng. (2025) 106926.
[16] M.A. Ezzat, A.S. El Karamany, M.A. Fayik, Fractional order theory in thermoelastic solid with three-phase-lag heat transfer, Arch. Appl. Mech. 82 (4) (2012) 557–572.
[17] A. Zada, U. Riaz, J. Jamshed, M. Alam, A. Kallekh, Analysis of impulsive Caputo fractional integro-differential equations with delay, Math. Methods Appl. Sci. 48 (2) (2025) 2102–2121.
[18] FRACTIONAL THERMOELASTICITY: A REVIEW. EasyChair Preprint2023.
[19] J. Ma, X. Yang, Y. Sun, J. Yang, Theoretical analysis on thermal treatment of skin with repetitive pulses, Sci. Rep. 11 (1) (2021) 9958, https://doi.org/10.1038/s41598-021-89395-x.
[20] Q. Zhang, Y. Sun, J. Yang, A.K. Soh, X. Wang, Theoretical analysis of thermal response in biological skin tissue subjected to multiple laser beams, Case Stud. Therm. Eng. 24 (2021) 100853, https://doi.org/10.1016/j.csite.2021.100853.
[21] N. Das, N. Sarkar, A. Lahiri, Reflection of plane waves from the stress-free isothermal and insulated boundaries of a nonlocal thermoelastic solid, Appl. Math. Model. 73 (2019) 526–544, https://doi.org/10.1016/j.apm.2019.04.028.
[22] N. Sarkar, S.K. Tomar, Plane waves in nonlocal thermoelastic solid with voids, J. Therm. Stress. 42 (5) (2019) 580–606, https://doi.org/10.1080/01495739.2018.1554395.
[23] G.A. Grinspan, S. Aguiar, N. Benech, Optimization of a surface wave elastography method through diffraction and guided waves effects characterization, J. Phys. Conf. Ser. 705 (2016) 012014, https://doi.org/10.1088/1742-6596/705/1/012014.
[24] S. Biswas, B. Mukhopadhyay, Eigenfunction expansion method to characterize Rayleigh wave propagation in orthotropic medium with phase lags, Waves Random Complex Media 29 (4) (2018) 722–742, https://doi.org/10.1080/17455030.2018.1470355.
[25] R. Tiwari, R. Kumar, Analysis of plane wave propagation under the purview of three-phase-lag theory of thermoelasticity with non-local effect, Eur. J. Mech. A/Solids 88 (2021) 104235.
[26] S. Debnath, S.S. Singh, Effect of thermal diffusivity on Rayleigh waves in human tissue, J. Vib. Control (2024), https://doi.org/10.1177/10775463241237360.
[27] Han, Z., Singh, M., Aglyamov, S.R., Liu, C.H., Nair, A., Raghunathan, R.,. And Larin, K.V.. Quantifying tissue viscoelasticity using optical coherence elastography and the Rayleigh wave model. *Journal of biomedical optics*, *21*(9), 090504-090504 (2016). https://doi.org/10.1117/1.JBO.21.9.090504.
[28] I.Z. Nenadic, M.W. Urban, S. Aristizabal, S.A. Mitchell, T.C. Humphrey, J. F. Greenleaf, On Lamb and Rayleigh wave convergence in viscoelastic tissues, Phys. Med. Biol. 56 (20) (2011) 6723–6738, https://doi.org/10.1088/0031-9155/56/20/014.
[29] M.A. Khan, M.M. Hemi, U. Riaz, W.F. Alfwzan, A. Jahangir, Boundary dependent sensitivity of thermo viscoelastic Rayleigh waves in skin tissue using a fractional nonlocal TPL framework, Mater. Des. 115836 (2026).
[30] S. Gupta, S. Das, R. Dutta, Influence of gravity, magnetic field, and thermal shock on mechanically loaded rotating FGDPTM structure under Green-Naghdi theory, Mech. Based Des. Struct. Mach. 51 (2) (2023) 764–792.
[31] S. Gupta, R. Dutta, S. Das, Photothermal excitation of an initially stressed nonlocal semiconducting double porous thermoelastic material under fractional order triple-phase-lag theory, Int. J. Numer. Methods Heat. Fluid Flow. 32 (12) (2022) 3697–3725.
[32] V. Gupta, H. Ahmad, M.S. Barak, S. Das, S. Kumar, Rayleigh wave in nonlocal piezo-thermo-electric semiconductor medium with fractional MGT model, Waves Random Complex Media (2024) 1–24.
[33] S. Das, A. Sur, V. Gupta, R. Dutta, A. Singhal, P. Kumar, Hydro-thermo-electromechanical response in a size-dependent porous piezoelectric medium under memory-dependent MGT theory, Mech. Adv. Mater. Struct. (2025) 1–21.
[34] A. Sur, K. Lotfy, N.K. Ranjit, S. Das, Advanced finite element analysis of photothermal response in cylindrical semiconductor with spatial nonlocality and memory-dependent heat transport, Int. Commun. Heat. Mass Transf. 169 (2025) 109771.
[35] I. Ullah, M.A. Khan, S.M. Abo-Dahab, A. Dar, M.R. Sial, M.D. Albalwi, A. Jahangir, Study on impact of variable thermal conductivity or laser pulse on reflected elastic waves in a semiconductor medium, Acoust. Phys. 70 (2) (2024) 278–287.
[36] M.A. Khan, A. Jahangir, A. Rahman, E.E. Mahmoud, M. Almuzaini, Global sensitivity analysis of wave behavior in rotating solids with laser-induced thermal and stress effects, Mech. Solids (2025) 1–24.
[37] M.A. Khan, A. Jahangir, S.B. Moussa, U. Riaz, M. Saqib, Rayleigh waves in graded thermoelastic media with fractional heat conduction: a sensitivity-based approach, Therm. Sci. Eng. Prog. (2026) 104564.
[38] D. Mehta, B. Betz-Stablein, T.D. Nguyen, Y. Gal, A. Bowling, M. Haskett, Z. Ge, Revamping AI models in dermatology: Overcoming critical challenges for enhanced skin lesion diagnosis, arXiv Prepr. arXiv *2311* (2023) *01009*.
[39] M.A. Khan, S.B. Moussa, A. Jahangir, U. Riaz, Microstructure-driven wave energy control in temperature-dependent fiber-reinforced composites: a unified micropolar thermoelastic model and data-driven design, Results Eng. (2025) 108811.
[40] D. Kumar, B. Paswan, P. Singh, J. Baroi, Rayleigh wave propagation in a rotating nonlocal micropolar thermoelastic composite structure: D. Kumar et al, Acta Mech. (2025) 1–27.
[41] E.L. Madsen, H.J. Sathoff, J.A. Zagzebski, Ultrasonic shear wave properties of soft tissues and tissuelike materials, J. Acoust. Soc. Am. *74* (5) (1983) 1346–1355.
[42] C.J. Diederich, K. Hynynen, Ultrasound technology for hyperthermia, Ultrasound Med. Biol. *25* (6) (1999) 871–887.